Computer Assisted Mechanics and Engineering Sciences, 7: 641–666, 2000.
Copyright © 2000 by Institute of Fundamental Technological Research, Polish Academy of Sciences

Adaptive ultimate load analysis of RC shells[1]

Roman Lackner and Herbert A. Mang
Institute for Strength of Materials, Vienna University of Technology
Karlsplatz 13, A-1040 Vienna, Austria

(Received November 3, 1999)

The aim of the present paper is a synthesis of both realistic modelling of the structural behavior of reinforced concrete (RC) shells and an adaptive finite element (FE) calculation tool suitable for the solution of nonlinear problems involving strain-hardening and softening plasticity. In the context of incremental-iterative analysis, an incremental error estimator is introduced. It is based on the rate of work. The reference solution required for error estimation is obtained by means of a recovery scheme applied to stress resultants. If the estimated error exceeds a prespecified threshold value, a new mesh is designed. Mesh generation is performed in the 2D parametric space of the shell. After mesh refinement, the state variables are transferred from the old to the new mesh and the calculation is restarted at the load level which was attained by the old mesh. The usefulness of the developed adaptive analysis scheme is demonstrated by a numerical analysis of an RC cooling tower.

1. INTRODUCTION

Approximately twenty years ago the first reports on ultimate load analysis of RC surface structures by the FEM appeared in the open literature. During the eighties significant progress was made in the field of constitutive modelling both in the precracking and the postcracking material domain as well as in the area of structural analysis of real-life civil engineering structures such as cooling towers, see, e.g., [5]. At this time, systematic investigations of the error of the results of such ultimate load analyses were unfeasible. At the best, the rate of convergence of the obtained results was estimated by means of uniform mesh refinement.

Beginning in the seventies, significant scientific efforts with regards to adaptive analysis were made. Originally, these efforts were directed towards linear analysis. The bulk of pertinent error estimators is based on modified versions of two approaches:

- The residual-type error estimator [1] employs
  - the difference in the tractions at common edges of finite elements, and
  - the forces resulting from local violation of the equilibrium equations for the discretized continuum.

  The displacements corresponding to the mentioned out-of-balance forces provide an estimate of the exact error.
- The second version of error estimators applies continuity conditions across element edges to each stress component [21]. For the estimation of the error, a smoothed (continuous) stress distribution is computed by post-processing the FE stresses. The difference between the FE stresses and the smoothed stresses, measured in an adequate norm, yields the estimated error.

For both modes of error estimation a spatial distribution of the error is obtained. Remeshing techniques exploit this information for the generation of an improved discretization characterized by

[1]Dedicated to Professor Yavuz Başar on the occasion of his 65th birthday

increasing the number of elements in regions of large error and decreasing this number in regions of small error. For this purpose, adaptive calculation schemes have been developed for automatic remeshing. At the beginning of such an adaptive calculation, usually a uniform FE mesh is generated. On the basis of the distribution of the estimated error new meshes are designed until a user-prescribed accuracy is reached.

After an extensive research in the linear range, adaptivity was extended to nonlinear analyses. The nonlinearity of the load–displacement relations either stems from the strain–displacement relations (*geometric nonlinearity*) or from the stress–strain relations (*material nonlinearity*). Nonlinear FE analyses are commonly solved by an incremental-iterative solution technique. This procedure allows to distinguish between two different types of error measures:

- *total* error measures which are computed from quantities taken from the entire load history applied so far, and

- *incremental* error measures employing quantities related to the considered increment.

Violation of the accuracy requirement at a certain load level leads to generation of a new mesh. Depending on the employed error measure, the calculation is either restarted at

- the beginning of the load history for the *total* error, or at
- the attained load level when employing an *incremental* error measure.

For the latter mode of restart, a transfer of variables from the old to the new mesh is required. In addition to the displacement field, the history variables have to be transferred for the case of elastoplastic material response.

The focus of the present paper is on the development of an adaptive FE procedure applicable to nonlinear shell analysis. Section 2 contains the definition of an error estimator accounting for elastoplastic material behavior. Further, the extension of error estimation to the layer concept, which is employed for the description of the mechanical behavior of reinforced concrete, is given. Section 3 deals with the design of the new mesh within the adaptive scheme. The transfer of variables from the old to the new mesh, which provides the initial conditions for the restart of the calculation, is treated in Section 4. In Section 5 the potential of the proposed calculation scheme is demonstrated numerically by means of a study of an RC cooling tower. In Section 6, a summary of this paper will be given. Moreover, conclusions drawn from the adaptive analysis of the RC cooling tower will be presented.

2. Error estimation in elastoplasticity

In the early nineties, researchers began applying adaptive calculation schemes to problems characterized by nonlinear material response. The underlying error estimators were obtained by

- modifying existing error estimators which were developed for the analysis of linear problems (see, e.g., [17, 11]), or

- adding error measures to existing error estimators which were developed for the analysis of linear problems (see, e.g., [2]). Such additional error measures account for the nonlinear material response.

Consistent with the evolution equations of the theory of plasticity, most of the proposed error estimators were introduced in rate form. The error, *total* or *incremental*, is obtained by time integration over the respective time interval.

2.1. Definition of an error measure

The error measure proposed in this paper is derived from the rate of work, $\dot{\mathcal{W}}$, defined as $\dot{\mathcal{W}} = \boldsymbol{\sigma}^T \dot{\boldsymbol{\varepsilon}}$, of the difference between the so-called recovered solution and the finite element solution[2]

$$\dot{\mathcal{W}}^{*-h} = \int_V \sum_{i,j=1}^{3} \left| \left(\sigma_{ij}^* - \sigma_{ij}^h\right) \left(\dot{\varepsilon}_{ij}^* - \dot{\varepsilon}_{ij}^h\right) \right| \mathrm{d}V \,. \tag{1}$$

The superscript "h" refers to the FE solution. The superscript "*" identifies the recovered solution obtained from smoothing of the FE solution within the framework of post-processing. The recovered solution is a substitute for the true solution which is unknown.

As regards ultimate load analysis of RC shells, the strains are usually small even close before reaching the ultimate load. Hence, a geometrically nonlinear theory restricted to small strains is adequate. The total strain tensor $\boldsymbol{\varepsilon}$ is decomposed into an elastic and a plastic part,

$$\boldsymbol{\varepsilon} = \boldsymbol{\varepsilon}^e + \boldsymbol{\varepsilon}^p \,. \tag{2}$$

Consideration of (2) in the expression of $\dot{\mathcal{W}}^{*-h}$ yields

$$\dot{\mathcal{W}}^{*-h} = \int_V \sum_{i,j=1}^{3} \left| \left(\sigma_{ij}^* - \sigma_{ij}^h\right) \left[\left(\dot{\varepsilon}_{ij}^{e,*} + \dot{\varepsilon}_{ij}^{p,*}\right) - \left(\dot{\varepsilon}_{ij}^{e,h} + \dot{\varepsilon}_{ij}^{p,h}\right) \right] \right| \mathrm{d}V \,. \tag{3}$$

It follows from Eq. (3), that three different error measures are contributing to $\dot{\mathcal{W}}^{*-h}$: the error in the total stresses, $\sigma_{ij}^* - \sigma_{ij}^h$, and the error in the elastic and plastic strain rate, $\dot{\varepsilon}_{ij}^{e,*} - \dot{\varepsilon}_{ij}^{e,h}$ and $\dot{\varepsilon}_{ij}^{p,*} - \dot{\varepsilon}_{ij}^{p,h}$. The latter two contributions might lead to an undesirable reduction of $\dot{\mathcal{W}}^{*-h}$ for different signs of $(\dot{\varepsilon}_{ij}^{e,*} - \dot{\varepsilon}_{ij}^{e,h})$ and $(\dot{\varepsilon}_{ij}^{p,*} - \dot{\varepsilon}_{ij}^{p,h})$. This fact is considered in the definition of the rate of the error estimator, $(\dot{e^2})$, where $\dot{\mathcal{W}}^{*-h}$ is splitted into an elastic and a plastic part, $\dot{\mathcal{W}}^{e,*-h}$ and $\dot{\mathcal{W}}^{p,*-h}$:

$$(\dot{e^2}) := \dot{\mathcal{W}}^{e,*-h} + \dot{\mathcal{W}}^{p,*-h} \tag{4}$$

with

$$\dot{\mathcal{W}}^{e,*-h} = \int_V \sum_{i,j=1}^{3} \left| \left(\sigma_{ij}^* - \sigma_{ij}^h\right) \sum_{k,l=1}^{3} \left[D_{ijkl} \left(\dot{\sigma}_{kl}^* - \dot{\sigma}_{kl}^h\right) \right] \right| \mathrm{d}V \tag{5}$$

and

$$\dot{\mathcal{W}}^{p,*-h} = \int_V \sum_{i,j=1}^{3} \left| \left(\sigma_{ij}^* - \sigma_{ij}^h\right) \left(\dot{\varepsilon}_{ij}^{p,*} - \dot{\varepsilon}_{ij}^{p,h}\right) \right| \mathrm{d}V \,. \tag{6}$$

D_{ijkl} represents the compliance tensor. It can easily be shown that the error measure proposed in Eq. (4) gives an upper bound of $\dot{\mathcal{W}}^{*-h}$, i.e.,

$$\dot{\mathcal{W}}^{*-h} \leq \dot{\mathcal{W}}^{e,*-h} + \dot{\mathcal{W}}^{p,*-h} =: (\dot{e^2}) \,. \tag{7}$$

By restricting the integrals in Eqs. (5) and (6) to the finite element k, the *local* (element) error rate, $(\dot{e_k^2})$, is obtained. Summation over the elements yields the *global* error rate as $(\dot{e^2}) = \sum_{k=1}^{m_e} (\dot{e_k^2})$, where m_e represents the number of elements of the actual finite element mesh.

An *incremental* error for the load increment $(n+1)$ associated with the time interval $[t_n, t_{n+1}]$ is obtained by time integration of the error rate (4),

$$\Delta(e^2)_{n+1} = \int_{t_n}^{t_{n+1}} (\dot{e^2}) \, \mathrm{d}t \,. \tag{8}$$

[2] In contrast to $\dot{\mathcal{W}}$, the expression on the right-hand side of (1) is no genuine physical quantity. This expression is defined such that all terms in the respective sum are positive quantities.

$\Delta(e^2)_{n+1}$ is computed by integration in space (see Eqs. (5) and (6)) and time (see Eq. (8)). Hence, its value depends on both the size of the considered structure and the chosen load incrementation. In the following, $\Delta(e^2)$ is referred to as *absolute* error measure. For adaptive analysis, a *relative* error measure, η, which neither depends on the size of the considered structure nor on the chosen load incrementation, is introduced. It is computed from the *absolute* error measure, $\Delta(e^2)$, and a reference quantity, $\Delta(u^{h,2})$,

$$\eta^2 = \frac{\Delta(e^2)}{\Delta(u^{h,2})} \,. \tag{9}$$

The definition of the rate of the reference quantity $\Delta(u^{h,2})$ follows from Eq. (4), yielding

$$(\dot{u^{h,2}}) := \dot{\mathcal{W}}^{e,h} + \dot{\mathcal{W}}^{p,h} \,, \tag{10}$$

with

$$\dot{\mathcal{W}}^{e,h} = \int_V \sum_{i,j=1}^{3} \left| \sigma_{ij}^h \sum_{k,l=1}^{3} \left[D_{ijkl} \dot{\sigma}_{kl}^h \right] \right| \mathrm{d}V \qquad \text{and} \qquad \dot{\mathcal{W}}^{p,h} = \int_V \sum_{i,j=1}^{3} \left| \sigma_{ij}^h \dot{\varepsilon}_{ij}^{p,h} \right| \mathrm{d}V \,. \tag{11}$$

The *relative local* (element) error η_k is obtained by replacing $\Delta(e^2)$ in Eq. (9) by the respective contribution of the considered element, i.e.,

$$\eta_k^2 = \frac{\Delta(e_k^2)}{\Delta(u^{h,2})} \,. \tag{12}$$

Summation over all elements of the FE mesh yields the *relative global* error $\eta^2 = \sum_{k=1}^{m_e} \eta_k^2$.

After error estimation, the *relative global* error η is compared to a user-prescribed error threshold value $\bar{\eta}$. The adaptive process, i.e., mesh refinement and restart of the calculation with the new mesh, is initiated if the threshold value is exceeded, i.e., if

$$\eta > \bar{\eta} \,. \tag{13}$$

2.2. Error estimation in the context of the incremental-iterative solution strategy

Time integration of the rate equations of the elastoplastic material law is performed by a backward Euler scheme as part of the incremental-iterative solution strategy. Hence, FE results are provided at the end of each load increment. Incremental changes within the $(n+1)$-st load increment, such as, e.g., stress increments, are computed from the respective values at t_n and t_{n+1}, i.e., $\Delta\boldsymbol{\sigma}_{n+1}^h = \boldsymbol{\sigma}_{n+1}^h - \boldsymbol{\sigma}_n^h$. Error estimation is performed after each load increment. The *absolute global* error $\Delta(e^2)$ and the reference quantity $\Delta(u^{h,2})$ for the $(n+1)$-st load increment are computed from

$$\begin{aligned} \Delta(e^2)_{n+1} = & \int_V \sum_{i,j=1}^{3} \left| \left(\sigma_{ij,n+1}^* - \sigma_{ij,n+1}^h \right) \sum_{k,l=1}^{3} \left[D_{ijkl} \left(\Delta\sigma_{kl,n+1}^* - \Delta\sigma_{kl,n+1}^h \right) \right] \right| \mathrm{d}V + \\ & + \int_V \sum_{i,j=1}^{3} \left| \left(\sigma_{ij,n+1}^* - \sigma_{ij,n+1}^h \right) \left(\Delta\varepsilon_{ij,n+1}^{p,*} - \Delta\varepsilon_{ij,n+1}^{p,h} \right) \right| \mathrm{d}V \,, \end{aligned} \tag{14}$$

and

$$\Delta(u^{h,2})_{n+1} = \int_V \sum_{i,j=1}^{3} \left| \sigma_{ij,n+1}^h \sum_{k,l=1}^{3} \left[D_{ijkl} \Delta\sigma_{kl,n+1}^h \right] \right| \mathrm{d}V + \int_V \sum_{i,j=1}^{3} \left| \sigma_{ij,n+1}^h \Delta\varepsilon_{ij,n+1}^{p,h} \right| \mathrm{d}V \,. \tag{15}$$

For the evaluation of $\boldsymbol{\sigma}^*_{n+1}$ and $\Delta\boldsymbol{\sigma}^*_{n+1}$, a smoothing algorithm enforcing continuity of stresses is employed [22]. For the simulation of localization such as cracking of concrete, the analytical solution exhibits jumps in the stress distribution (see, e.g., [8]). Accordingly, the aforementioned continuity conditions for the stresses employed during stress recovery is replaced by a continuity condition for the tractions [8]. The error in the incremental plastic strains, $\Delta\boldsymbol{\varepsilon}^{p,*}_{n+1} - \Delta\boldsymbol{\varepsilon}^{p,h}_{n+1}$, is computed from the yield criterion. For a detailed description of both procedures the reader is referred to [10].

2.3. Extension of error estimation to the layer concept

For the simulation of the mechanical behavior of RC plates and shells, the layer concept is employed (see Fig. 1).

For the extension of error estimation to the layer concept, stress resultants such as the axial force $\mathbf{n}^h$ and the bending moment $\mathbf{m}^h$ are computed from the FE stresses according to their definitions given in Fig. 2. Afterwards, the stress recovery scheme is applied to $\mathbf{n}^h$ and $\mathbf{m}^h$, yielding $\mathbf{n}^*$ and $\mathbf{m}^*$. The recovered stresses $\boldsymbol{\sigma}^*$ are determined from $\mathbf{n}^*$ and $\mathbf{m}^*$ by means of an extreme value problem with two constraint conditions. This problem is formulated for each stress component at each integration point, using Lagrangian multipliers λ_n and λ_m,

$$\mathcal{F}(\hat{\sigma}^{1,*}_{ij}, \dots \hat{\sigma}^{n,*}_{ij}; \lambda_n, \lambda_m) = \sum_{\ell=1}^{n} \left(\hat{\sigma}^{\ell,*}_{ij} - \hat{\sigma}^{\ell,h}_{ij}\right)^2 + \lambda_n \left(\hat{n}^*_{ij} - \frac{h}{2}\sum_{\ell=1}^{n} \hat{\sigma}^{\ell,*}_{ij}\Delta\xi^\ell\right) + \lambda_m \left(\hat{m}^*_{ij} + \frac{h^2}{4}\sum_{\ell=1}^{n} \hat{\sigma}^{\ell,*}_{ij}\xi^\ell\Delta\xi^\ell\right) \longrightarrow \text{stationary}. \tag{16}$$

In Eq. (16), n denotes the number of layers, h is the thickness, and ξ is a normalized coordinate orthogonal to the middle surface of the shell (see Fig. 2). Values at the considered integration point are indicated by the symbol " $\hat{}$ ".

Application of the same procedure to the increments of the axial force, $\Delta\mathbf{n}^h$, and the bending moment, $\Delta\mathbf{m}^h$, yields the required stress increments $\Delta\boldsymbol{\sigma}^*$.

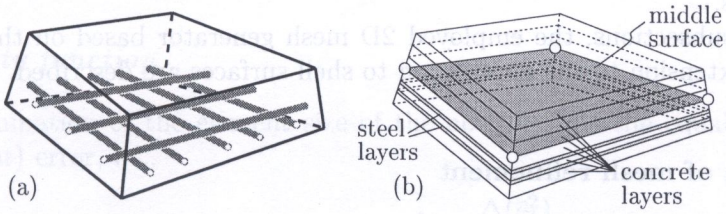

Fig. 1. Consideration of reinforcement: (a) real situation and (b) consideration of the reinforcement by steel layers

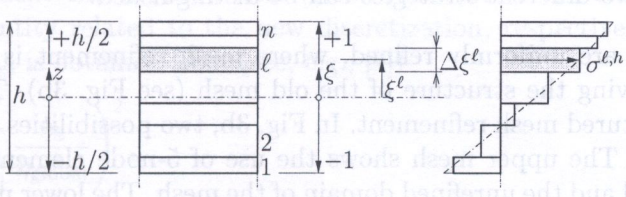

Fig. 2. Layer concept with piecewise constant stress distribution for the simulation of composite surface structures. Computation of stress resultants.

3. Generation of a new mesh

If the error criterion is violated, i.e., if $\eta > \bar{\eta}$, the actual discretization has to be modified. The FEM offers two basic possibilities of mesh adaption. One of them is change of the element size. The other one is change of the degree of the interpolation polynomials in the approximation for the element displacements. Based on these two possibilities of mesh adaption, several refinement techniques were proposed. They are referred to as:

1. the h-version, where the element size is adapted during the design of a new mesh,
2. the p-version, where the degree of the interpolation polynomials (shape functions) in the approximation for the element displacements is changed, and
3. the r-version, moving node points without changing the element connectivity and, consequently, the number of degrees of freedom.

The combination of the h-version and the p-version is referred to as the hp-version [4].

The selection of the appropriate refinement technique depends on the kind of problem under consideration. For error-controlled analysis of elastoplastic shells, the basic requirements for mesh generation are:

- high flexibility as regards element shape and orientation of the element edges which allows an improved representation of plastic deformations by the FE discretization,
- design of well-shaped elements even for the case of rapid changes of, e.g., the element size for the case of the h-version of mesh refinement, and
- satisfaction of the error criterion by the new discretization, i.e., $\eta \leq \bar{\eta}$.

Since no change in the element connectivity is performed in the r-version of mesh refinement, it neither has the required flexibility nor does it provide well-shaped elements. Moreover, because of the fixed number of nodes, the error criterion is not necessarily satisfied by the new mesh. On the other hand, the increase of the order of the interpolation polynomial in the context of the p-version of mesh refinement does not reduce the error for the case of discontinuous stress and strain distributions, such as observed during the simulation of elastoplastic material response [8]. The h-version of mesh refiment shows the highest flexibility and, hence, is well-suited for the application to adaptive elastoplastic analysis.

In the following subsections, the employed 2D mesh generator based on the h-version of mesh refinement and its extension to the application to shell surfaces are described.

3.1. The h-version of mesh refinement

The design of a new mesh on the basis of the h-version of mesh refinement is characterized by adapting the element size according to the spatial distribution of a refinement indicator. In error-controlled mesh adaption, the *local* (element) error is commonly used as such an indicator. Within the h-version of mesh refinement, two different strategies can be distinguished:

- In the first one, finite elements are uniformly refined, where mesh refinement is signalled by the *local* (element) error, conserving the structure of the old mesh (see Fig. 3b). This mode of refinement is referred to as structured mesh refinement. In Fig. 3b, two possibilities of structured mesh refinement are illustrated. The upper mesh shows the use of 5-node elements to achieve compatibility between the refined and the unrefined domain of the mesh. The lower mesh contains standard element configurations consisting of 4-node elements to achieve the aforementioned compatibility. Obviously, for both modes of structured mesh refinement, the orientation of the

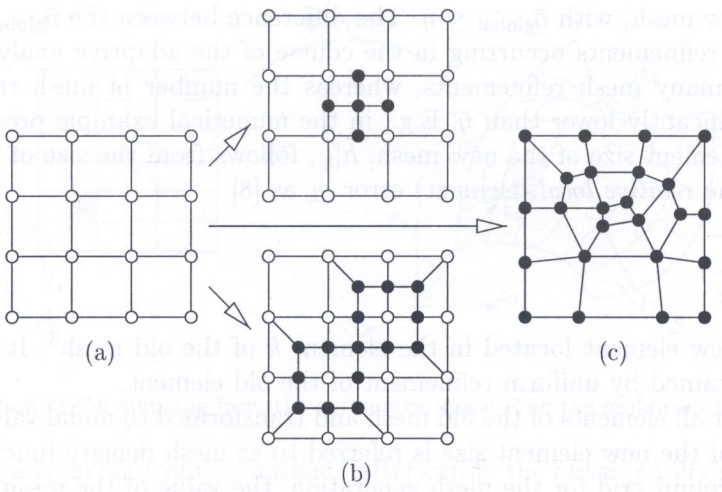

Fig. 3. Illustration of the h-version of mesh refinement: (a) old mesh, (b) new meshes obtained from structured mesh refinement, and (c) new mesh obtained from unstructured mesh refinement

element sides of the new elements is defined by the structure of the old mesh and cannot be prescribed by the user.

In the course of structured mesh refinement, one element of the old mesh may be divided into 2×2, 3×3, $\ldots n\times n$ new elements. Hence, the possible options for the size of the new element are given by the size of the old element, h_k, and the number of new elements, namely $h_k/2$, $h_k/3$, $\ldots h_k/n$.

- The second mode of h-version of mesh refinement is based on unstructured meshes (see Fig. 3c). Hereby, a new mesh, i.e., one with new nodal coordinates and new element connectivity, is designed. Information concerning the new element size is provided by the so-called mesh density function, $\bar{h}(\mathbf{x})$, which is computed from the distribution of the *local* (element) error.

In this work, the unstructured mesh refinement technique is employed. In contrast to structured mesh refinement, it allows the adaption of the orientation of the element edges. Moreover, the size of the new elements corresponds almost exactly to the respective value of the mesh density function.

In what follows, the evaluation of the mesh density function, $\bar{h}(\mathbf{x})$, and the advancing front method are described. This technique is commonly used in unstructured mesh refinement.

3.1.1. Mesh density function

The basis for determination of the element size of the new mesh is the equal distribution of the *relative local* (element) error, i.e.,

$$\bar{\eta}_1 = \bar{\eta}_2 = \ldots = \bar{\eta}_k = \ldots = \bar{\eta}_{\bar{m}_e} \hat{=} \bar{\eta}_{\text{local}} \qquad \text{with} \quad \bar{\eta}_k^2 = \frac{\Delta(\bar{e}_k^2)}{\Delta(\bar{u}^{h,2})}\,, \tag{17}$$

where $\bar{\eta}_k$ denotes the *relative local* (element) error of the element k of the new mesh. $\Delta(\bar{e}_k^2)$ and $\Delta(\bar{u}^{h,2})$ represent the *absolute local* (element) error of the element k of the new mesh and the reference quantity related to the new discretization, respectively. The number of elements of the new mesh, $\bar{m}_e$, is obtained from (see, e.g., [9])

$$\bar{m}_e = \left(\sum_{k=1}^{m_e} \frac{\eta_k}{\bar{\eta}_{\text{global}}} \right)^2, \tag{18}$$

where m_e is the number of elements of the old mesh and η_k is the *relative local* (element) error related to the element k of the old mesh. In Eq. (18), $\bar{\eta}_{\text{global}}$ represents the user-defined *relative*

global error of the new mesh, with $\bar{\eta}_{\text{global}} \leq \bar{\eta}$. The difference between the $\bar{\eta}_{\text{global}}$ and $\bar{\eta}$ is related to the number of mesh refinements occurring in the course of the adaptive analysis. Values of $\bar{\eta}_{\text{global}}$ close to $\bar{\eta}$ result in many mesh refinements, whereas the number of mesh refinements decreases for $\bar{\eta}_{\text{global}}$ being significantly lower than $\bar{\eta}$. E.g., in the numerical example presented in this paper, $\bar{\eta}_{\text{global}} = 0.8\bar{\eta}$. The element size of the new mesh, $\bar{h}|_k$, follows from the size of the element k of the old mesh, h_k, and the *relative local* (element) error η_k as [8]

$$\bar{h}|_k = h_k \sqrt{\frac{\bar{\eta}_{\text{global}}}{\sqrt{\bar{m}_e}\eta_k}} \,. \tag{19}$$

$\bar{h}|_k$ is the size of a new element located in the element k of the old mesh[3]. It is assumed that the new elements are obtained by uniform refinement of the old element.

$\bar{h}|_k$ is evaluated for all elements of the old mesh and transformed to nodal values. The so-obtained spatial distribution of the new element size is referred to as mesh density function, $\bar{h}(\mathbf{x})$. With the old mesh as a background grid for the mesh generation, the value of the mesh density function, $\bar{h}$, can be obtained at every point of the domain.

3.1.2. The advancing front technique

A widely used algorithm for the design of an unstructured mesh is based on the *advancing front technique* [16]. The front is defined as the border between refined and unrefined subdomains. After refinement of the boundary representing the front at the beginning of mesh refinement (see Fig. 4a), single quadrilateral elements are generated (see Fig. 4b). For both refinement of the boundary and element design, the mesh density function is employed to control the size of the new elements. The algorithm terminates after the front, which finally has four sides, is closed by an element (see Fig. 4c). Generally, the refinement procedure is completed by mesh improvement and node relaxation algorithms [20].

A detailed description of the individual steps of the refinement process and the consideration of mesh alignment, i.e., the orientation of the element edges according to a user-defined criterion, is given in [9].

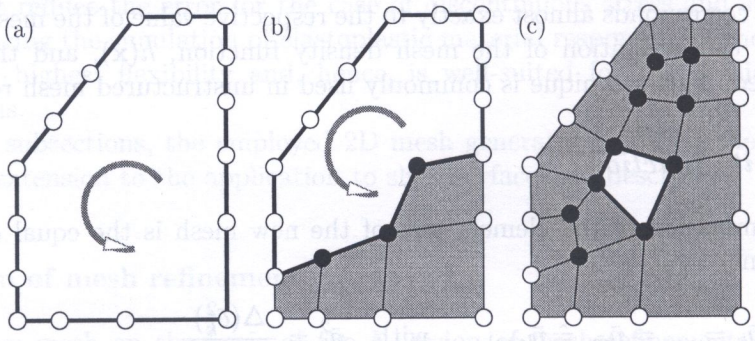

Fig. 4. Short illustration of the advancing front technique: (a) refinement of the boundary of the domain according to the spatial distribution of the local (element) error, (b) process of element design and, finally, (c) closure of the front by the last element

3.2. Extension to $2^1/_2$D surface structures

For the generation of meshes for $2^1/_2$D surface structures, the parametric space of the surface, $\mathcal{A}$ (with $\mathcal{A} \subset \mathbb{R}^2$), is employed (see Fig. 5). The FE mesh is designed in the parametric space using

[3]The used notation $\bar{h}|_k$ should not be confused with $\bar{h}_k$ which denotes the size of the element k of the new mesh.

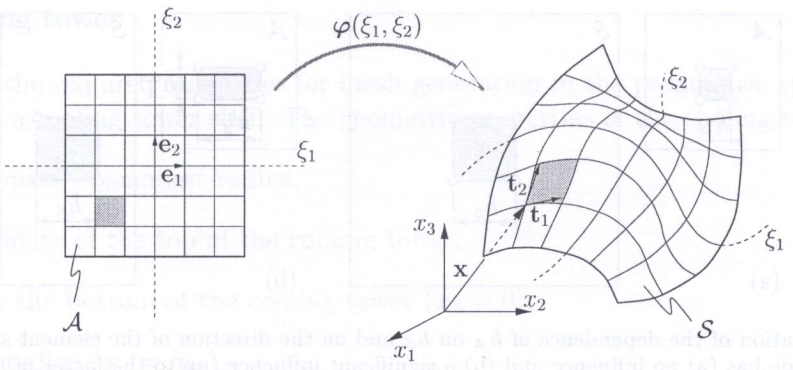

Fig. 5. Illustration of the mapping from the parametric space $\mathcal{A}$ to the middle surface of the shell $\mathcal{S}$

the earlier described advancing front technique. Afterwards, the obtained 2D mesh is mapped onto the middle surface of the shell, $\mathcal{S}$ (with $\mathcal{S} \subset \mathbb{R}^3$). The mapping is described by a mapping function φ, given by

$$\mathbf{x} = \varphi(\xi_1\,,\,\xi_2)\,, \tag{20}$$

where $(\xi_1\,,\,\xi_2) \in \mathbb{R}^2$ are the local coordinates of the parametric space. The mapping function is assumed to be regular, i.e.,

$$\frac{\partial \mathbf{x}}{\partial \xi_1} \times \frac{\partial \mathbf{x}}{\partial \xi_2} \neq \mathbf{0} \tag{21}$$

for all points on $\mathcal{S}$. The partial derivatives in Eq. (21) represent the tangent vectors at the point $\mathbf{x}$ of the shell surface $\mathcal{S}$, given by

$$\mathbf{t}_1 = \frac{\partial \mathbf{x}}{\partial \xi_1} \quad \text{and} \quad \mathbf{t}_2 = \frac{\partial \mathbf{x}}{\partial \xi_2}\,. \tag{22}$$

The vectors $\mathbf{t}_1$ and $\mathbf{t}_2$ are the columns of the functional matrix $\mathbf{J}$

$$\mathbf{J} = [\mathbf{t}_1\,,\,\mathbf{t}_2]\,. \tag{23}$$

$\mathbf{J}$ is employed for the determination of the metric tensor $\mathbf{G}$, defined by

$$\mathbf{G}(\xi_1\,,\,\xi_2) = \begin{bmatrix} g_{11} & g_{12} \\ g_{21} & g_{22} \end{bmatrix} = \mathbf{J}^T(\xi_1\,,\,\xi_2)\,\mathbf{J}(\xi_1\,,\,\xi_2)\,. \tag{24}$$

$\mathbf{G}$ is symmetric. In the following the influence of mappings on the design of elements in the parametric space is investigated.

Change in size:

The mesh density function on the shell surface $\mathcal{S}$ is a scalar function with given values at the nodes of the old mesh. Each value of $\bar{h}_{\mathcal{S}}$ only depends on the location on the shell surface. The respective value in the parametric space $\mathcal{A}$ also depends on the considered direction in which the element size is required. Figure 6 illustrates the dependence of the mesh density function in $\mathcal{A}$ on the direction for two example problems. For the left case, which is characterized similar shapes of $\mathcal{A}$ and $\mathcal{S}$, the value of the mesh density function at the considered point is $\bar{h}_{\mathcal{A}} = \bar{h}_{\mathcal{S}}/2$ and equal for the horizontal and the vertical direction. In the right example, $\mathcal{A}$ and $\mathcal{S}$ have different shapes. For this example, $\bar{h}_{\mathcal{A}}$ in the horizontal direction is equal to $\bar{h}_{\mathcal{S}}$, whereas $\bar{h}_{\mathcal{A}}$ in the vertical direction is given by $\bar{h}_{\mathcal{A}} = \bar{h}_{\mathcal{S}}/2$. In the course of mesh generation, the mesh density function controls the size of the element sides and, hence, the direction of the respective element side is used for the evaluation of $\bar{h}_{\mathcal{A}}$. Such a direction is given by the unit vector in the parametric space, $\mathbf{a}_{\mathcal{A}}$,

$$\mathbf{a}_{\mathcal{A}} = a_1\mathbf{e}_1 + a_2\mathbf{e}_2 \qquad \text{with} \quad |\mathbf{a}_{\mathcal{A}}| = 1\,, \tag{25}$$

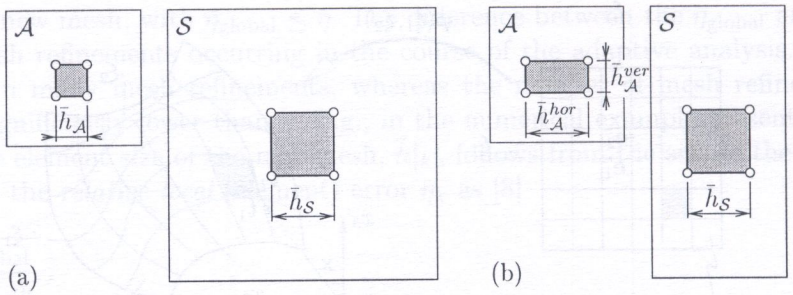

Fig. 6. Illustration of the dependence of $\bar{h}_{\mathcal{A}}$ on $\bar{h}_{\mathcal{S}}$ and on the direction of the element side: direction of element side has (a) no influence and (b) a significant influence (up to the factor of two) on $\bar{h}_{\mathcal{A}}$

where $\mathbf{e}_1$ and $\mathbf{e}_2$ denote the unit vectors in the directions of the local coordinates ξ_1 and ξ_2 in $\mathcal{A}$. The transformation of the vector $\mathbf{a}_{\mathcal{A}}$ on the shell surface yields

$$\mathbf{a}_{\mathcal{S}} = a_1 \mathbf{t}_1 + a_2 \mathbf{t}_2 \,. \tag{26}$$

The scaling of the mesh density function evaluated for the direction of $\mathbf{a}_{\mathcal{A}}$ is obtained as the length of $\mathbf{a}_{\mathcal{S}}$,

$$\frac{\bar{h}_{\mathcal{S}}}{\bar{h}_{\mathcal{A}}} = \frac{|\mathbf{a}_{\mathcal{S}}|}{|\mathbf{a}_{\mathcal{A}}|} = |\mathbf{a}_{\mathcal{S}}| \,, \tag{27}$$

where $\bar{h}_{\mathcal{S}}$ and $\bar{h}_{\mathcal{A}}$ are the values of the mesh density function on the surface and in the parametric space, respectively.

Change in angle:

Mesh generation is performed in the parametric space $\mathcal{A}$. However, the directions of element edges for the design of well-shaped elements or the consideration of mesh alignment are specified on $\mathcal{S}$. Hence, the problem arising during mesh generation can be formulated as follows: *Find the components of the vector* $\mathbf{b}_{\mathcal{A}}$ *(unit vector in the unknown direction) for a known vector* $\mathbf{a}_{\mathcal{A}}$ *(unit vector in the known direction) and a prescribed angle on the shell surface,* $\alpha_{\mathcal{S}} = \mathrm{ang}(\mathbf{a}_{\mathcal{S}}, \mathbf{b}_{\mathcal{S}})$. $\alpha_{\mathcal{S}}$ is given by

$$\cos \alpha_{\mathcal{S}} = \frac{\mathbf{a}_{\mathcal{S}}^T \mathbf{b}_{\mathcal{S}}}{|\mathbf{a}_{\mathcal{S}}||\mathbf{b}_{\mathcal{S}}|} \,. \tag{28}$$

For the evaluation of the unknown components of the vector $\mathbf{b}_{\mathcal{A}}$, b_1 and b_2,

$$\mathbf{a}_{\mathcal{S}} = a_1 \mathbf{t}_1 + a_2 \mathbf{t}_2 \qquad \text{and} \qquad \mathbf{b}_{\mathcal{S}} = b_1 \mathbf{t}_1 + b_2 \mathbf{t}_2 \tag{29}$$

are substituted into Eq. (28). The so-obtained nonlinear equation for b_1 and b_2 is solved in an iterative manner. The second equation required is given by

$$|\mathbf{b}_{\mathcal{A}}| = \sqrt{b_1^2 \mathbf{e}_1^T \mathbf{e}_1 + b_2^2 \mathbf{e}_2^T \mathbf{e}_2} = \sqrt{b_1^2 + b_2^2} = 1. \tag{30}$$

For the special case of $\alpha_{\mathcal{S}} = \pi/2$, i.e., $\mathbf{a}_{\mathcal{S}}^T \mathbf{b}_{\mathcal{S}} = 0$, analytical expressions for the unknown vector $\mathbf{b}_{\mathcal{A}}$ can be derived (see [18]).

Change in area:

For the evaluation of the integrals employed in error estimation, the parametric space is considered. Therefore, the differential of the surface area, $\mathrm{d}A_{\mathcal{S}}$, is replaced by (see, e.g., [12])

$$\mathrm{d}A_{\mathcal{S}} = \sqrt{g_{11}\, g_{22} - g_{12}\, g_{21}}\, \mathrm{d}A_{\mathcal{A}} \,, \tag{31}$$

where $\mathrm{d}A_{\mathcal{A}}$ denotes the differential of the surface area in the parametric space.

Example: Cooling tower

The evaluation of the required quantities for mesh generation in the parametric space is illustrated for the example of a cooling tower shell. The geometric properties of the cooling tower are given by

h_m – x_3-coordinate of smallest radius,

h_t – x_3-coordinate of the top of the cooling tower,

r_b – radius at the bottom of the cooling tower ($x_3 = 0$),

r_m – smallest radius ($x_3 = h_m$).

The axis of rotation is coinciding with the x_3-coordinate axis. The surface of the cooling tower is given in the (x_1, x_2, x_3)-coordinate system by

$$x_1 = r\cos\xi_1\,, \qquad x_2 = r\sin\xi_1 \qquad \text{and} \qquad x_3 = \xi_2 h_t/(2\pi)\,, \tag{32}$$

with

$$r(x_3) = r_m\sqrt{1 + \left(\frac{r_b^2}{r_m^2} - 1\right)\frac{(x_3 - h_m)^2}{h_m^2}}\,. \tag{33}$$

In Eq. (32), ξ_1 and ξ_2 refer to the circumferential and meridional parametric coordinate, respectively. The size of the parametric space is given by $-\pi \le \xi_1 \le \pi$ and $0 \le \xi_2 \le 2\pi$. For the description of one half of the cooling tower the range of ξ_1 is reduced to $0 \le \xi_1 \le \pi$. The tangent vectors on the surface of the shell are given by

$$\mathbf{t}_1 = \frac{\partial \mathbf{x}}{\partial \xi_1} = \left\{ \begin{array}{c} -r\sin\xi_1 \\ r\cos\xi_1 \\ 0 \end{array} \right\} \tag{34}$$

and

$$\mathbf{t}_2 = \frac{\partial \mathbf{x}}{\partial \xi_2} = \left\{ \begin{array}{c} (\partial x_1/\partial r)\,(\partial r/\partial x_3)\,(\partial x_3/\partial \xi_2) \\ (\partial x_2/\partial r)\,(\partial r/\partial x_3)\,(\partial x_3/\partial \xi_2) \\ (\partial x_3/\partial \xi_2) \end{array} \right\} = \frac{h_t}{2\pi}\left\{ \begin{array}{c} r'\cos\xi_1 \\ r'\sin\xi_1 \\ 1 \end{array} \right\}, \tag{35}$$

where

$$r' = \frac{\mathrm{d}r}{\mathrm{d}x_3} = \frac{r_m^2}{r}\left(\frac{r_b^2}{r_m^2} - 1\right)\frac{x_3 - h_m}{h_m^2}\,. \tag{36}$$

The evaluation of the metric tensor $\mathbf{G}$ yields $g_{12} = g_{21}$=0. The remaining entries of the metric tensor are given by

$$g_{11} = \mathbf{t}_1^T\mathbf{t}_1 = r^2\,, \qquad g_{22} = \mathbf{t}_2^T\mathbf{t}_2 = \left[\frac{h_t}{2\pi}\right]^2\left[1 + (r')^2\right]. \tag{37}$$

The scaling function for the element size is computed using $\mathbf{t}_1^T\,\mathbf{t}_2 = 0$ and Eqs. (34) and (35),

$$\frac{\bar{h}_{\mathcal{S}}}{\bar{h}_{\mathcal{A}}} = |\mathbf{a}_{\mathcal{S}}| = |a_1\mathbf{t}_1 + a_2\mathbf{t}_2| = \sqrt{(a_1\mathbf{t}_1 + a_2\mathbf{t}_2)^T(a_1\mathbf{t}_1 + a_2\mathbf{t}_2)} = \sqrt{a_1^2\mathbf{t}_1^T\mathbf{t}_1 + a_2^2\mathbf{t}_2^T\mathbf{t}_2}$$
$$= \sqrt{a_1^2 r^2 + a_2^2\left[\frac{h_t}{2\pi}\right]^2\left[1 + (r')^2\right]}\,. \tag{38}$$

The required relation between the differential of the surface area and the differential in the parametric space is given by

$$\mathrm{d}A_{\mathcal{S}} = \frac{r h_t}{2\pi}\sqrt{1+(r')^2}\,\mathrm{d}A_{\mathcal{A}}\,. \tag{39}$$

Figure 7 contains the obtained uniform[4] discretization of a cooling tower shell with the following dimensions: $h_m = 59.00$ m, $h_t = 82.00$ m, $r_b = 27.40$ m, $r_m = 17.72$ m. Additionally, a separation line at $x_3 = 8.44$ m is introduced. At this line a change in the mode of reinforcement from two reinforcement grids to one grid occurs. Figure 7a shows the obtained mesh of the cooling tower when neglecting the aforementioned dependence of $\bar{h}_{\mathcal{S}}/\bar{h}_{\mathcal{A}}$ on ξ_2 (see Eq. (38)). $\bar{h}_{\mathcal{A}}$ is assumed to be constant which results in elements of similar size in the parametric space $\mathcal{A}$ and, hence, different element sizes on the shell surface $\mathcal{S}$. An improved discretization is obtained using a variable value of $\bar{h}_{\mathcal{A}}$ computed from a prescribed constant value $\bar{h}_{\mathcal{S}}$ according to Eq. (38) resulting in similar element sizes on the shell surface $\mathcal{S}$ (see Fig. 7b).

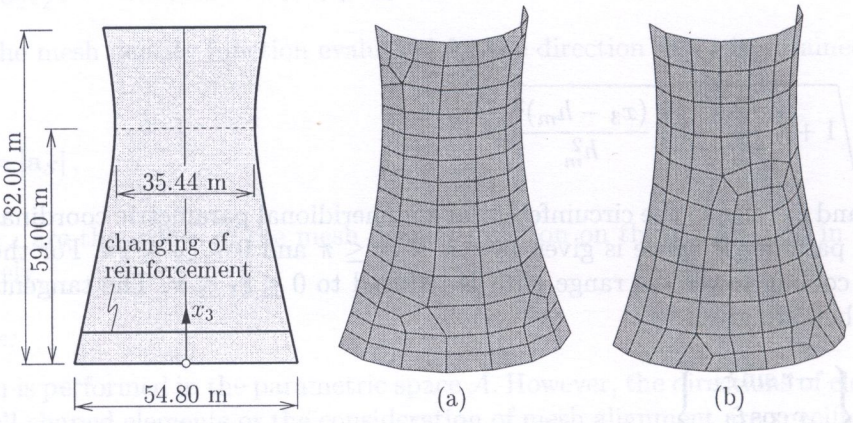

Fig. 7. Uniformly generated meshes of a cooling tower shell with the aim of a constant element size on the shell surface, i.e., $h_{\mathcal{S}}$=constant: (a) based on $\bar{h}_{\mathcal{A}}$ = constant leading to elements of different size on $\mathcal{S}$, and (b) based on $\bar{h}_{\mathcal{S}}$ = constant ($\bar{h}_{\mathcal{A}}$ is computed from Eq. (38)) leading to a uniform mesh on $\mathcal{S}$

4. Restart of the Calculation. Transfer of Variables from the Old to the New Mesh

As regards the restart of the calculation after mesh refinement, two major strategies are possible:

(a) the calculation is restarted at the beginning of the load history, i.e., at $t = 0$, or

(b) the calculation is restarted at the load level attained by the old mesh, i.e., at $t = t_n$.

The first approach is characterized by reconsideration of the entire load history applied so far which would be prohibitively expensive for large-scale analyses. Hence, the second approach will be used. This approach requires the transfer of variables from the old to the new mesh. It provides the initial condition for the restart of the computation after mesh refinement.

In addition to the displacement field $\mathbf{u}$, history variables such as the plastic strains $\boldsymbol{\varepsilon}^p$ and the internal variables $\boldsymbol{\alpha}$ must be transferred for the case of elastoplastic material behavior (see Fig. 8). In general, the quantities of the new mesh obtained from the transfer of variables do not yield an equilibrated state, i.e., $\mathbf{F}^{\text{ext}}_{\text{new}} - \mathbf{F}^{\text{int}}_{\text{new}}(\boldsymbol{\sigma}_{\text{new}}) \neq \mathbf{0}$, where $\mathbf{F}^{\text{ext}}$ and $\mathbf{F}^{\text{int}}$ denote the vector of external and internal forces, respectively. Hence, a global equilibrium iteration must be performed. Especially,

[4]The term "uniform" refers to the size of the finite elements only. Thus, uniformly generated meshes consist of finite elements of approximately equal size.

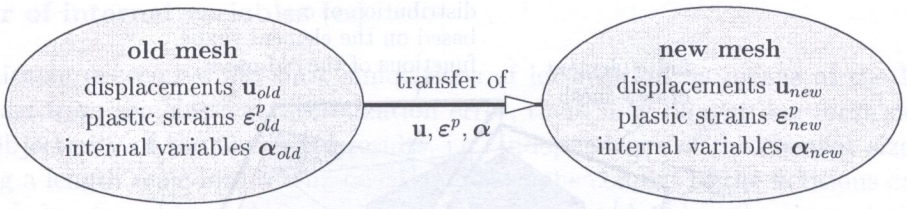

Fig. 8. On the evaluation of the initial quantities for the new mesh: transfer of displacements $\mathbf{u}$ and history variables $\boldsymbol{\varepsilon}^p$ and $\boldsymbol{\alpha}$

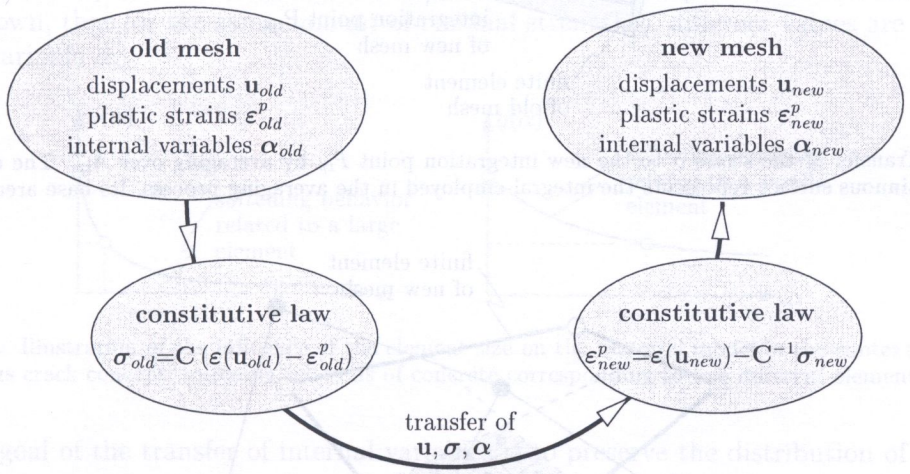

Fig. 9. On the evaluation of the initial quantities for the new mesh: transfer of displacements $\mathbf{u}$, stresses $\boldsymbol{\sigma}$ and internal variables $\boldsymbol{\alpha}$. $\mathbf{C}$ denotes the material matrix

the transfer of the two kinematic quantities $\mathbf{u}$ and $\boldsymbol{\varepsilon}^p$ as illustrated in Fig. 8 may lead to stress states which are far away from equilibrium. This results in a deterioration of the convergence behavior of the equilibrium iteration.

The rate of convergence of this iteration is improved considerably if the stress field is transferred instead of the plastic strains [7] (see Fig. 9). The non-transferred plastic strains are computed from the transferred displacements and stresses by means of the constitutive law. In the following, the transfer scheme illustrated in Fig. 9, will be described in detail.

4.1. Transfer of stresses ($\boldsymbol{\sigma}$)

Initial stress states are required at the integration points of the new mesh. Herein, averaging the stresses from the old mesh over the proportionate area of the considered integration point P_{ip} is proposed for the evaluation of the new stress state (see Fig. 10)

$$\sigma_{\text{new}} = \frac{1}{A_{ip}} \int_{A_{ip}} \sigma_{\text{old}}(\mathbf{x})\, \mathrm{d}A\,. \tag{40}$$

A_{ip} denotes the domain related to the integration point P_{ip}. σ_{old} is given at the integration points of the old mesh. Its spatial distribution is obtained by interpolation and extrapolation on the basis of the element shape functions. In general, this distribution is discontinuous across element edges (see Fig. 10) and, hence, a numerical approach seems to be appropriate for the determination of the integral in Eq. (40). It is characterized by dividing the integration point area, A_{ip}, into $n \times n$ subareas, $A_{ip}^{(ij)}$, with $i, j = 1, 2 \ldots n$ (see Fig. 11). Within each subarea, the value of σ_{old}

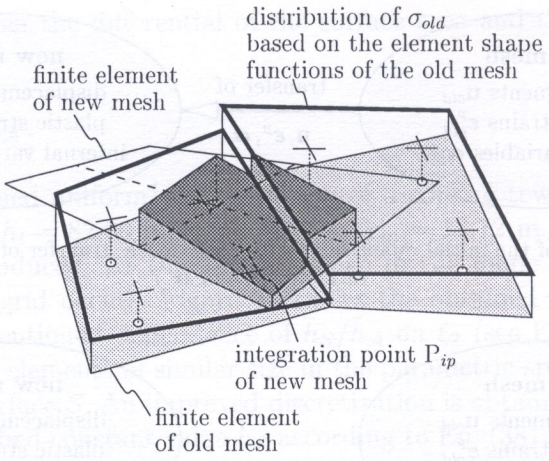

Fig. 10. Transfer of the stress σ to the new integration point P_{ip} by averaging over A_{ip}. The dark-shaded discontinuous surface represents the integral employed in the averaging process. Its base area is A_{ip}

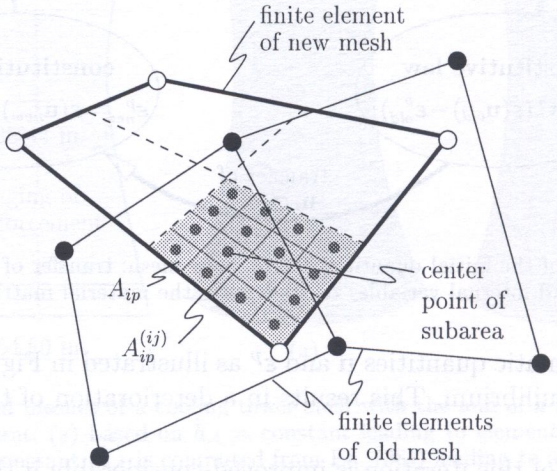

Fig. 11. Illustration of the numerical integration scheme for the transfer of stresses. Division of the integration point area A_{ip} into 4×4 subareas

is set constant, corresponding to $\sigma_{\text{old}}(\mathbf{x})$ evaluated at the center point of the respective subarea, $\sigma_{\text{old}}(\mathbf{x}_{center}^{(ij)})$. Thus, an approximation of the integral in Eq. (40) is obtained as

$$\int_{A_{ip}} \sigma_{\text{old}}(\mathbf{x}) \mathrm{d}A \quad \longrightarrow \quad \sum_{i=1}^{n} \sum_{j=1}^{n} A_{ip}^{(ij)} \sigma_{\text{old}}(\mathbf{x}_{\text{center}}^{(ij)}) \,. \tag{41}$$

The transfer scheme for the stresses is further improved by transferring the recovered stress distribution obtained in the course of error estimation instead of the FE stresses of the old mesh. Moreover, an additional stress recovery is performed on the new mesh. The result of the latter recovery is then employed for the evaluation of the plastic strains at the integration points of the new mesh by means of the constitutive law.

4.2. Transfer of displacements (u)

The displacement field for the new mesh is obtained by means of interpolation using the element shape functions.

4.3. Transfer of internal variables (α)

Without a suitable preventive measure, simulations of localization by means of the FEM are not objective. Apart from the classical discretization error, there may be a strong mesh dependence of the results. Objectivity of the numerical results, i.e., independence of the element size, is achieved by introducing a length scale into the material model. In the context of the fictitious crack concept, this length scale is referred to as characteristic length ℓ_c. It is related to the element size. Figure 12 contains softening relations used for the simulation of concrete under tensile loading showing the exponential degradation of the residual strength $\bar{q}$ as a function of the internal variable α. The plotted curves correspond to two different element sizes and, consequently, to two different values of ℓ_c. It is shown, that for the same amount of residual strength $\bar{q}$, different values are obtained for the internal variable α.

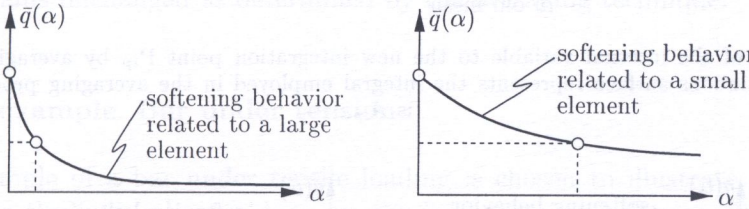

Fig. 12. Illustration of the influence of the element size on the material model in the context of the fictitious crack concept: softening relations of concrete corresponding to two different element sizes

The main goal of the transfer of internal variables is to preserve the distribution of the residual strength of the material, $\bar{q}$, during the transfer. As illustrated in Fig. 12, $\bar{q}$ depends on both the internal variable α and the element size expressed through the characteristic length ℓ_c. Averaging techniques used in the context of the transfer of state variables consider contributions of different finite elements of the old mesh for the evaluation of the value at the integration point of the new mesh (see, e.g., Fig. 10). Consequently, any influence of the element size on the value of the internal variable must be eliminated before averaging can be performed. Accordingly, the characteristic length ℓ_c, which is computed from the size of the finite element, is replaced by a constant arbitrary reference length $\bar{\ell}_c$ (see Fig. 13). This results in similar softening relations for all elements of all meshes designed in the course of the adaptive analysis. During the transfer of internal variables the earlier described averaging technique is applied to the internal variable related to $\bar{\ell}_c$, $\bar{\alpha}$. Hence, the value of $\bar{\alpha}$ at the integration point of the new mesh is obtained by

$$\bar{\alpha}_{\text{new}} = \frac{1}{A_{ip}} \sum_{i=1}^{n} \sum_{j=1}^{n} A_{ip}^{(ij)} \bar{\alpha}_{\text{old}}(\mathbf{x}_{\text{center}}^{(ij)}) \,. \tag{42}$$

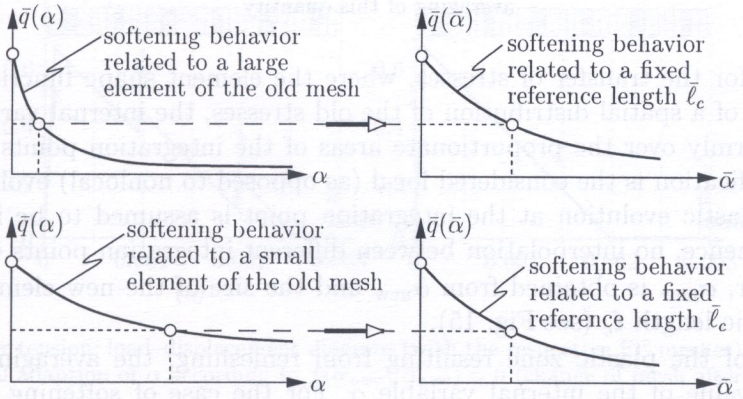

Fig. 13. Transfer of internal variables: elimination of the influence of the element size on the evaluation of $\bar{q}$ by means of a constant arbitrary reference length $\bar{\ell}_c$

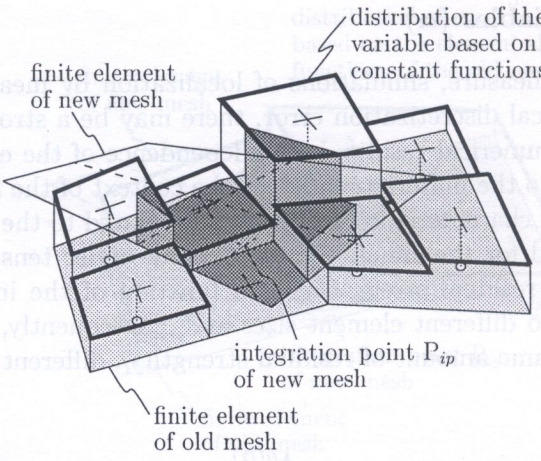

Fig. 14. Transfer of the internal variable to the new integration point P_{ip} by averaging over A_{ip}. The dark-shaded discontinuous surface represents the integral employed in the averaging process. Its base area is A_{ip}

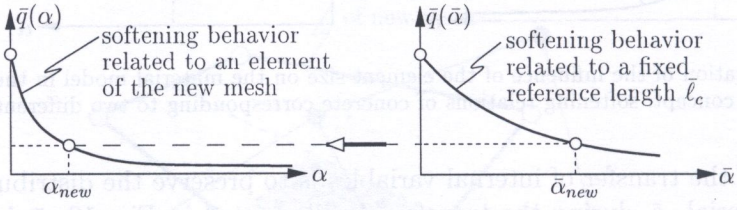

Fig. 15. Transfer of internal variables: evaluation of α_{new} by relating the residual strength obtained from the transfer of $\bar{\alpha}$, $\bar{q}(\bar{\alpha})$, to the size of the new finite element

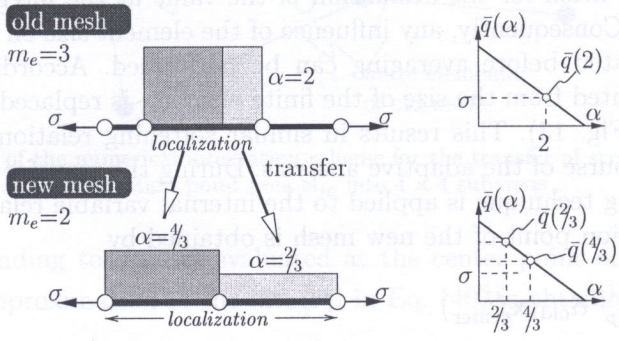

Fig. 16. Investigation of the nature of the deficiency of the transfer of the internal variable α by means of averaging of this quantity

However, unlike as for the transfer of stresses, where the element shape functions were employed for the construction of a spatial distribution of the old stresses, the internal variable is assumed to be distributed uniformly over the proportionate areas of the integration points (see Fig. 14). The reason for this modification is the considered local (as opposed to nonlocal) evolution of the plastic deformation. The plastic evolution at the integration point is assumed to be independent of the neighborhood and, hence, no interpolation between different integration points can be performed.

After the transfer, α_{new} is obtained from $\bar{\alpha}_{\text{new}}$ and the size of the new element represented by the new characteristic length ℓ_c (see Fig. 15).

For an increase of the plastic zone resulting from remeshing, the averaging technique yields a reduction of the value of the internal variable α. For the case of softening material behavior, this results in an artificial increase of the residual strength and, hence, of the elastic material domain. Figure 16 contains an illustrative 1D example used for the explanation of the reason for

this deficiency. The old mesh is assumed to consist of three linear truss elements (with one integration point each, located in the center of the element). The new mesh is assumed to consist of two finite elements. Localization is assumed to occur in the center element of the old mesh. The value of the internal variable is chosen as $\alpha = 2$. Transferring the internal variable[5] α to the new mesh by means of averaging, the distribution of α, which was restricted to one element of the old mesh, is extended to both elements of the new mesh. Obviously, an extension of the localization zone leads to a decrease of the value of the internal variable α. Hence, "artificial hardening" takes place. It results in stress states located within the increased elastic domain. This leads to a retrieval of elastic stiffness.

This deficiency was the motivation for an improvement of the proposed transfer scheme by adapting the internal variable to the respective yield condition, i.e., computing it from $f(\boldsymbol{\sigma}_{\text{new}}, \alpha_{\text{new}}) = 0$. For yield functions evaluated for domains of the old mesh without plastic loading, characterized by $f_{\text{old}} < 0$, α_{new} remains unchanged as determined by the averaging technique.

4.4. Illustrative example. Bar under tension

The academic example of a bar under tensile loading is chosen to illustrate the influence of the transfer scheme for the internal variable α on the load-carrying behavior. Therefore, refinement is initiated after equal intervals of the prescribed displacement. The influence of restarting the computation at a certain load level is investigated on the basis of the load–displacement diagram. For comparison, the proposed transfer scheme is applied without as well as with the additional adaption of the internal variable according to the yield condition $f(\boldsymbol{\sigma}_{\text{new}}, \alpha_{\text{new}}) = 0$.

The geometric dimensions and the material properties are given in Fig. 17. The stress–strain diagram in the softening regime is assumed as bilinear. It is calibrated according to the fictitious crack concept. The simulation is carried out under displacement control. The mesh is adapted after

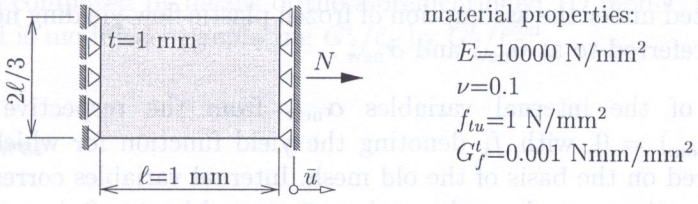

Fig. 17. Bar under tension: geometric dimensions and material properties

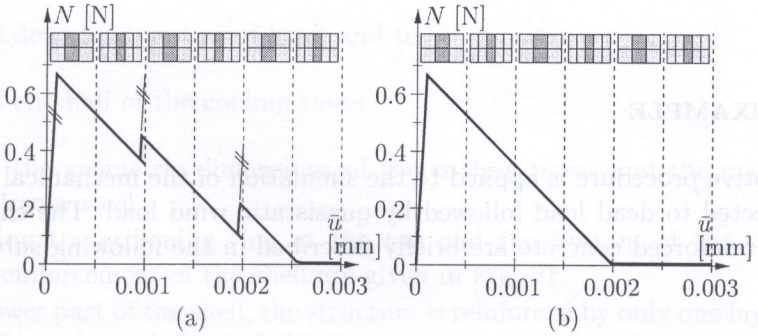

Fig. 18. Bar under tension: load–displacement diagram (with the respective FE meshes) for (a) without and (b) with additional adaption of α according to $f(\boldsymbol{\sigma}_{\text{new}}, \alpha_{\text{new}}) = 0$ (change of mesh after $\Delta\bar{u} = 0.0005$ mm)

[5]For the sake of simplification of the present example, for all elements of the old and the new mesh with localization the same length was chosen. Hence, no relation of α to a fixed reference length $\bar{\ell}_c$ is required.

equal intervals of the prescribed displacement ($\Delta\bar{u} = 0.0005$ mm). No error estimation is performed for this example. The chosen meshes and their sequence of application are illustrated in Fig. 18. The purpose of this sequence is to simulate the change of the size of the plastic zone. The onset of localization is triggered by the tensile strength f_{tu} in the elements containing the center of the bar (dark-shaded elements in Fig. 18).

Figure 18 contains the obtained load–displacement curves. For the averaging technique without the additional adaption of α, the extension of the plastic zone in the context of coarsening of the mesh leads to a stiffening of the structural response caused by a retrieval of elastic material behavior in the dark-shaded elements.

Box 1 summarizes the different steps of the proposed transfer scheme.

Box 1. Transfer of state variables from the old to the new mesh

1. Transfer of $\mathbf{u}_{\text{old}}$ to the new mesh by interpolation using the element shape functions and the nodal displacements of the old mesh, yielding $\mathbf{u}_{\text{new}}$.
2. Determination of internal variables $\boldsymbol{\alpha}_{\text{new}}$ and stresses $\boldsymbol{\sigma}_{\text{new}}$ at the integration points of the new mesh based on an averaging scheme characterized by numerical integration.
3. Smoothing of transferred stresses $\boldsymbol{\sigma}_{\text{new}}$ on the new mesh, giving $\boldsymbol{\sigma}^*_{\text{new}}$.
4. Evaluation of plastic strains $\boldsymbol{\varepsilon}^p_{\text{new}}$ according to the value of $\boldsymbol{\alpha}_{\text{new}}$,
   (a) $\boldsymbol{\varepsilon}^p_{\text{new}} = \mathbf{0}$ for $\boldsymbol{\alpha}_{\text{new}} = \mathbf{0}$ and
   (b) $\boldsymbol{\varepsilon}^p_{\text{new}} = \boldsymbol{\varepsilon}(\mathbf{u}_{\text{new}}) - \mathbf{C}^{-1}\boldsymbol{\sigma}^*_{\text{new}}$ for $\boldsymbol{\alpha}_{\text{new}} \neq \mathbf{0}$.
5. In order to decrease the unbalance of the internal forces introduced by the transfer of variables, a zero-load increment is applied. As initial data, $\mathbf{u}_{\text{new}}$ and $\boldsymbol{\varepsilon}^p_{\text{new}}$ are used. This step is computed under the assumption of frozen plastic flow yielding new displacements and stresses, referred to as $\tilde{\mathbf{u}}_{\text{new}}$ and $\tilde{\boldsymbol{\sigma}}_{\text{new}}$.
6. Modification of the internal variables $\boldsymbol{\alpha}_{\text{new}}$ from the respective yield criterion, $f_k(\tilde{\boldsymbol{\sigma}}_{\text{new}}, \tilde{\alpha}_{k,new}) = 0$, with f_k denoting the yield function for which plastic loading was encountered on the basis of the old mesh. Internal variables corresponding to non-active yield functions remain unchanged as computed in step 2, i.e., $\tilde{\alpha}_{k,new} = \alpha_{k,new}$.
7. Application of the next load increment using $\tilde{\mathbf{u}}_{\text{new}}$, $\boldsymbol{\varepsilon}^p_{\text{new}}$, and $\tilde{\boldsymbol{\alpha}}_{\text{new}}$ as initial quantities.

5. Numerical example

The described adaptive procedure is applied to the simulation of the mechanical behavior of an RC cooling tower subjected to dead load followed by quasistatic wind load. The characteristics of the material model for reinforced concrete are briefly described in the following subsection (for details see [6]).

5.1. Plasticity model for reinforced concrete

The different mechanical behavior of concrete in tension and compression is taken into account by the multi-surface plasticity concept (see Fig. 19). The Drucker–Prager yield criterion is used for the

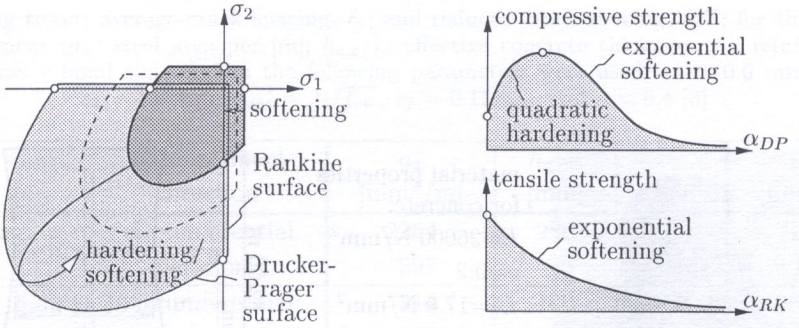

(a) yield surfaces (b) hardening/softening laws

Fig. 19. Illustration of the employed multi-surface model for the simulation of plain concrete: (a) yield surfaces in the principal stress space and (b) hardening/softening relations

simulation of the ductile response in compression. The Rankine criterion serves for the description of cracking.

For the description of the mechanical behavior of steel, a 1D model is used. It refers to the strain component in the direction of the steel bar.

In reinforced concrete, usually several cracks develop until a stabilized crack pattern is formed. The distribution of the cracks depends on the geometric properties such as bar diameter, concrete cover, etc. The average spacing between the visible (primary) cracks of this pattern, ℓ_s, is computed from the distribution of bond slip along the reinforcement bar. Therefore, a 1D composite model consisting of the reinforcement bar and the related concrete area is employed [6]. The value of ℓ_s is considered during the calibration of the material model for concrete such that the area under the exponential softening curve of the tensile strength (see Fig. 19(b)) is equal to the ratio of the fracture energy and the average crack spacing, i.e., G_f^t/ℓ_s. For consideration of the increase in the released strain energy because of bond slip and the development of secondary cracks, a reduced crack spacing, ℓ_s^{red}, is computed by means of the aforementioned 1D model. Hence, the calibration of the concrete model is modified by replacing G_f^t/ℓ_s by $G_f^t/\ell_s^{\text{red}}$.

5.2. RC cooling tower

The topic of analysis is the cooling tower III Ptolemaïs SES in Greece. The present analysis of this cooling tower is restricted to

- the assumption that the shell is undamaged at the beginning of the simulation,
- consideration of dead load and wind load, and to
- consideration of one half of the cooling tower.

Figure 20 contains the geometric dimensions of the cooling tower and the material properties of concrete and cold-drawn steel.

Details concerning the stiffening ring at the top and the bottom of the shell as well as the thickness and the reinforcement of the shell are given in Fig. 21.

Except for the lower part of the shell, the structure is reinforced by only one layer of reinforcement located in the middle surface of the shell. With the exception of the aforementioned lower part, the thickness of the shell is 0.10 m.

For the support columns (b/d = 0.40/0.50 m), linear elastic material behavior (E = 26000 N/mm^2 and ν = 0.2) is assumed. The parameters used for the consideration of the steel–concrete-interaction are given in Table 1.

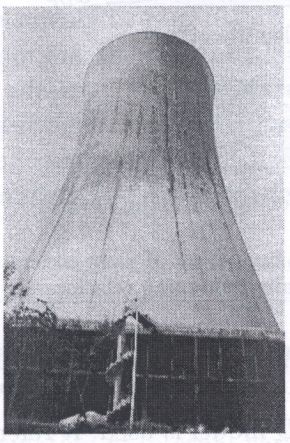

material properties
for concrete:
E=26000 N/mm^2
ν=0.2
f_{cu}=17.0 N/mm^2
f_{tu}=1.99 N/mm^2
G_f^c=3.75 Nmm/mm^2
G_f^t=0.075 Nmm/mm^2

material properties
for steel:
E=200000 N/mm^2
f_{sy}=400 N/mm^2

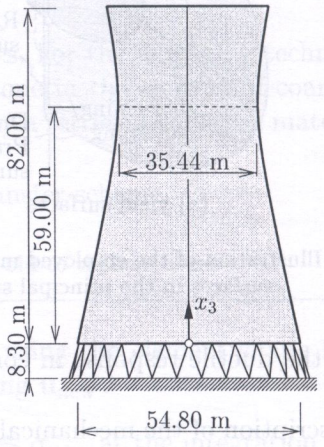

Fig. 20. Cooling tower III Ptolemaïs SES: geometric dimensions of the cooling tower; material properties of concrete and steel [15]

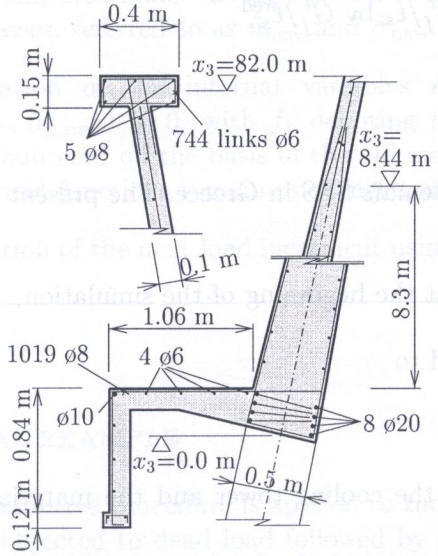

thickness of the shell [m]	
$x_3 \leq$12.65 m	t=0.1+0.4$\left(\frac{12.65-x_3}{12.65}\right)^{1.75}$
$x_3 >$12.65 m	t=0.1

reinforcement of the shell					
from x_3 [m]	to x_3 [m]	$\varnothing_m$ [mm]	n_m [1]	$\varnothing_c$ [mm]	e_c [m]
0.00	5.52	10	1019	10	0.25
5.52	8.44	10	1019	8	0.33
8.44	43.00	10	1083	8	0.33
43.00	52.00	10	713	8	0.33
52.00	60.26	10	558	8	0.25
60.26	68.56	10	560	8	0.25
68.56	82.00	10	350	8	0.33

Fig. 21. Cooling tower: geometric dimensions of the stiffening ring at the top and at the bottom, respectively, of the shell; tables containing information about the thickness and the meridional (subscript "m") and circumferential (subscript "c") reinforcement of the shell (n_m : number of meridional reinforcement bars; e_c : spacing of circumferential reinforcement)

Table 1. Cooling tower: average crack spacing, ℓ_s; and reduced crack spacing, ℓ_s^{red}; for the horizontal and vertical reinforcement (a_s : steel area per [m]; $h_{c,eff}$: effective concrete thickness; ρ_s: reinforcement ratio). For the bond stress – bond slip relation the following parameters were used: $s_1 = 0.6$ mm, $s_2 = 0.6$ mm, $s_3 = 1.0$ mm, $\tau_{\max} = 2\sqrt{f_{cu}}$, $\tau_f = 0.15\tau_{\max}$ and $\alpha = 0.4$ [3]

from x_3 [m]	to x_3 [m]	reinforcement direction	a_s [mm^2/m]	$h_{c,\text{eff}}$ [mm]	ρ_s [%]	ℓ_s [mm]	ℓ_s^{red} [mm]
bottom ring		circumferential	2254	280	0.81	715	67
		meridional	297	73	0.41	501	65
0.00	5.52	circumferential	314	100	0.31	664	82
		meridional	477	75	0.64	483	59
5.52	8.44	circumferential	151	95	0.16	1243	49
		meridional	497	75	0.66	477	59
8.44	43.00	circumferential	151	28	0.54	485	64
		meridional	636	28	2.27	61	56
43.00	52.00	circumferential	151	28	0.54	444	59
		meridional	491	28	1.75	287	55
52.00	60.26	circumferential	201	28	0.72	391	56
		meridional	393	28	1.40	333	53
60.26	68.56	circumferential	201	28	0.72	391	56
		meridional	393	28	1.40	333	53
68.56	82.00	circumferential	151	28	0.54	444	59
		meridional	235	28	0.84	428	55
top ring		circumferential	314	75	0.42	496	64
		meridional	172	70	0.25	507	89

The dead load of reinforced concrete is taken as $g = 25$ kN/m^3. In accordance with [19], the distribution of the quasi-static wind load w is assumed as

$$w(z, \Theta) = c_p(\Theta)\, q_E(z)\,, \tag{43}$$

where $c_p(\Theta)$ characterizes the circumferential distribution of the wind load and $q_E(z)$ denotes the pressure distribution over the heigth of the cooling tower. The circumferential distribution of the wind load is given as (curve K1.3 of [19])

$$c_p(\Theta) = \begin{cases} 1 - 2.3\left(\sin\frac{90}{73}\Theta\right)^{2.166} & \dots \quad 0 \le \Theta \le 73^\circ\,, \\ -1.3 + 0.8\left(\sin\frac{90}{24}(\Theta - 73)\right)^{2.395} & \dots \quad 73^\circ \le \Theta \le 96^\circ\,, \\ -0.5 & \dots \quad 96^\circ \le \Theta\,, \end{cases} \tag{44}$$

where $\Theta = 0^\circ$ is the direction of the wind. The vertical distribution of the wind pressure is given by [19] as

$$q_E(z) = \bar{q}\left(\frac{z}{10}\right)^{0.22} \qquad \text{with} \quad z = x_3 + 8.3 \text{ [m]}, \tag{45}$$

where $\bar{q}$ is used as the reference wind load. It represents the wind pressure acting at $z = 10$ m and $\Theta = 0^\circ$. In the simulation, at first the gravity load g is applied. Then, the wind load $\bar{q}$ is increased until the collapse of the cooling tower is signalled by the analysis.

During mesh generation, the element sides of the shell elements connected to the support columns are kept equal to the distance of the column heads. Otherwise the point-wise support of the shell would introduce singularities in the stress field resulting in continuous mesh refinement and, hence, in an undesirably high mesh density at $x_3 = 0$.

For the discretization of the shell, the layered (thick) shell element (element 75 of MARC element library [14]) is employed. In this analysis, the thickness of the shell is divided into 13 layers.

5.3. Results obtained by uniformly refined meshes

In this subsection, results from single-mesh (i.e., non-adaptive) calculations based on uniformly refined meshes are presented. The six discretizations, on which these results are based, are ranging from 74 to 1897 finite elements (see Fig. 22). For all meshes, the size of the element sides at the bottom stiffening ring is the same to provide compatibility between the discretization of the shell and the support columns.

The obtained load–displacement curves are shown in Fig. 23. u refers to the radial displacement component of a shell point located 61 m above the bottom ring at $\Theta=0°$. Convergence of the collapse

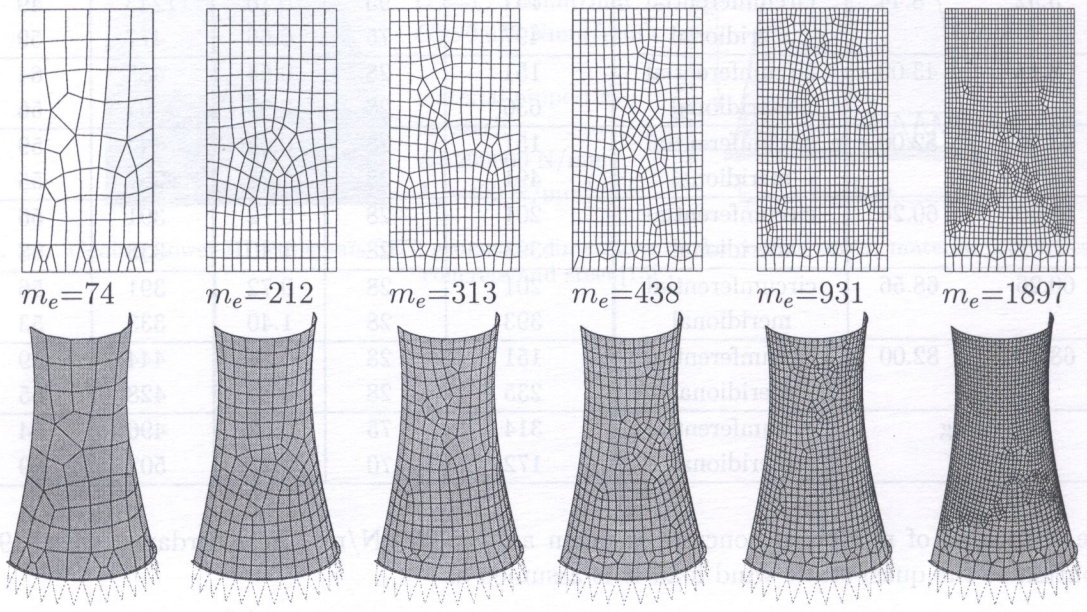

Fig. 22. Cooling tower: uniform finite element meshes used for single-mesh calculations (m_e : number of elements)

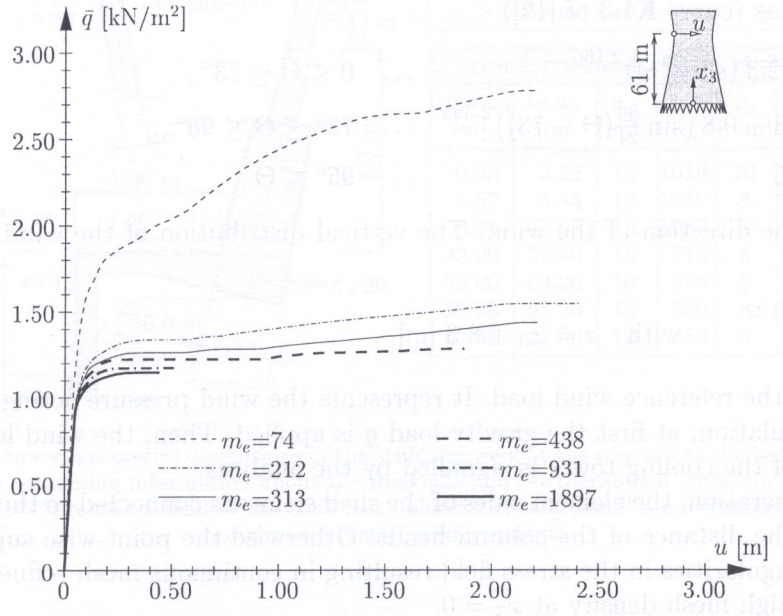

Fig. 23. Cooling tower: load–displacement diagrams for the radial displacement u from single-mesh calculations using uniform meshes (m_e : number of elements)

load is observed. For coarse meshes (m_e = 74, 212, 313, and 438), restiffening of the structural response is observed, leading to an overestimation of the collapse load. For the two finest meshes, m_e = 931 and m_e = 1897, the cooling tower fails because of vanishing structural stiffness which presumably is the correct failure mode.

5.4. Results obtained from adaptive FE analyses

The error threshold value for the adaptive calculation described in this subsection is specified as $\bar{\eta}$ = 10%. The error value employed for the design of the new mesh, $\bar{\eta}_{\text{global}}$, is given by $0.8\bar{\eta}$. Both error estimation and mesh refinement in the course of the adaptive analyis are performed in the parametric (2D) space of the shell (for details see [6]).

Altogether nine FE meshes were designed by the computer in the course of the adaptive calculation. As the initial (first) mesh, a uniform mesh, consisting of 73 finite elements, was taken (see Fig. 24). No mesh refinement occurred after application of dead load. The wind load, however, resulted in an increase of the error and, hence, in several mesh refinements. The new meshes are characterized by a greater mesh density at the windward side of the cooling tower.

Figure 25a contains the load–displacement curve obtained from adaptive analysis. Similar to the situation for the fine meshes in Fig. 23 (m_e = 931 and m_e = 1897), the vanishing of the structural stiffness seems to be the reason for the failure of the cooling tower. The wind load at collapse is obtained as $\bar{q}_u$ = 1.15 kN/m^2. The plotted load–displacement curve consists of contributions of all meshes used. Remarkably, the load–displacement curve does not contain discontinuities at loading states at which the mesh was refined. This reflects the small influence of the proposed transfer of

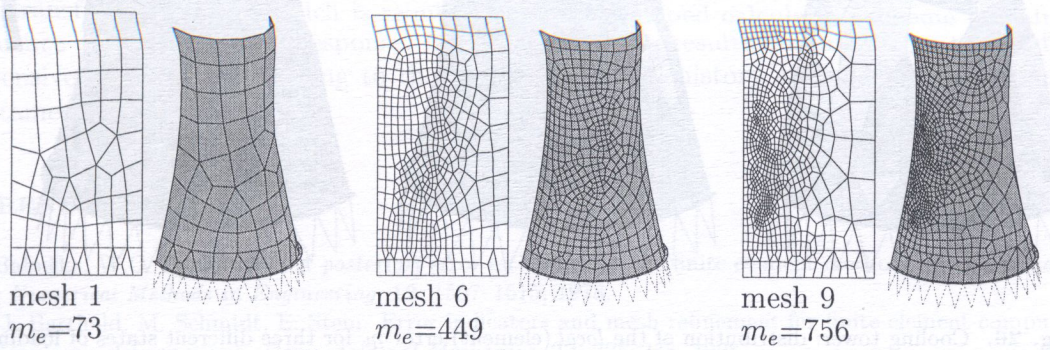

Fig. 24. Cooling tower: first (initial), sixth, and ninth (final) mesh generated in the course of adaptive ultimate load analysis based on $\bar{\eta}$ = 10% (m_e : number of elements)

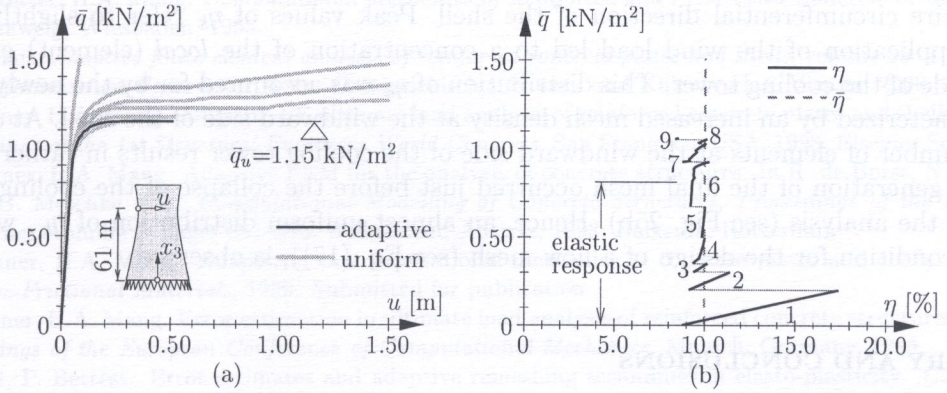

Fig. 25. Cooling tower: (a) load–displacement curve and (b) evolution of η obtained from the adaptive calculation based on $\bar{\eta}$ = 10%

variables from the old to the new mesh on the structural response. This is a desirable goal for such a transfer scheme.

The error evolution is shown in Fig. 25b. For the error analysis the finite elements of the stiffening rings and the support columns were disregarded. Application of the dead load, i.e., $\bar{q} = 0$, gave an error of $\eta = 8.8\%$. No further mesh refinement was required. Consideration of the wind load led to a change of the load-carrying behavior of the shell from axisymmetric behavior to symmetric behavior with respect to the plane $\Theta = 0°$. This resulted in an increase of η and, thus, in several mesh refinements. The sixth mesh (see Fig. 24) was found to meet the prescribed accuracy for the load combination of dead load and proportionally increasing wind load. At a wind load of approximately $\bar{q} = 0.81$ kN/m^2 another change in the load-carrying behavior of the shell was reflected by the evolution of η. At this load level, cracking of concrete and yielding of steel led to a reduction of the bending stiffness of the shell. The reduced load-carrying capacity in bending resulted in an increase of the membrane forces in the shell. Several adaptions of the FE mesh were required until the collapse load of the cooling tower was reached. This occurred for the ninth mesh.

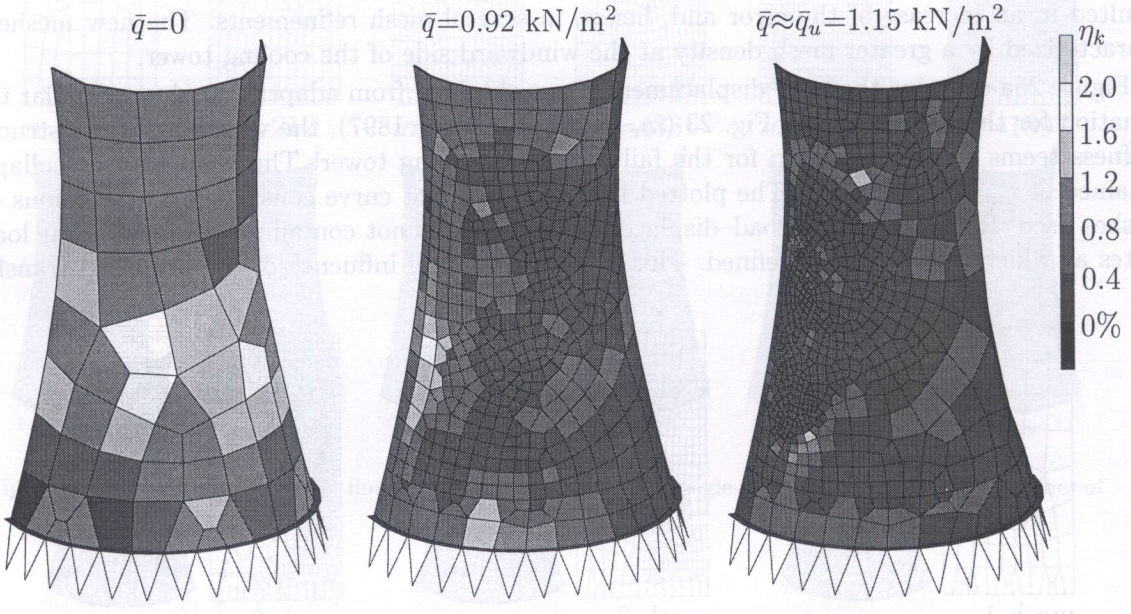

Fig. 26. Cooling tower: distribution of the *local* (element) error η_k for three different states of loading

Figure 26 shows the development of the *local* (element) error, η_k, for three different loading states. After application of dead load, a rather uniform distributed *local* (element) error is observed over the entire circumferential direction of the shell. Peak values of η_k refer to slightly distorted elements. Application of the wind load led to a concentration of the *local* (element) error at the windward side of the cooling tower. This distribution of η_k was accounted for by the newly generated meshes characterized by an increased mesh density at the windward side of the shell. At $\bar{q} \approx \bar{q}_u$, the increased number of elements at the windward side of the cooling tower results in rather low values of η_k. Mesh generation of the final mesh occurred just before the collapse of the cooling tower was signalled by the analysis (see Fig. 25b). Hence, an almost uniform distribution of η_k, which is the underlying condition for the design of a new mesh (see Eq. (17)), is observed.

6. Summary and conclusions

This paper has dealt with error estimation and adaptive mesh refinement in the context of ultimate load analysis of RC structures. The main items can be summarized as follows:

- As regards to error estimation, the error estimator was derived from the rate of work of the difference between the recovered solution and the FE result. The recovered solution was computed by means of a stress recovery scheme. The extension of error estimation to the layer concept, which was used for the simulation of the mechanical behavior of reinforced concrete surface structures, was accomplished by the recovery of stress resultants. The respective stresses were evaluated from the recovered stress resultants by means of an extreme value problem.

- For the generation of the new mesh, the advancing front technique was employed. The mesh density function, which contains the element size of the new mesh, was obtained from the condition of an equal distribution of the *local* (element) error. The extension of mesh generation to $2^1/_2$D surface structures was accomplished by mapping to the 2D parametric space of the surface allowing mesh refinement in this space.

- As for the calculation strategy, a restart scheme for continuation of the calculation at the attained load level was developed. The success of this strategy depends on the transfer algorithm of the state variables providing the initial state for the new mesh. In this paper, a transfer of the displacements, the stresses, and the internal variables was performed. The initial state of the plastic strains was computed by means of the constitutive law. Further, an additional update of the internal variable on the basis of the yield criterion was performed.

From the numerical investigation of an RC cooling tower the following conclusions can be drawn:

- As regards adaptive analysis, intelligent remeshing leads to a considerable reduction of the number of finite elements for results of comparable quality as the ones obtained from uniform mesh refinement.

- The transfer of variables which is required for the developed calculation scheme has almost no influence on the structural response. A comparison with results obtained from the by far more expensive strategy of returning to the begin of the load history after each mesh refinement is contained in [13].

REFERENCES

[1] I. Babuška, W.C. Rheinboldt. *A posteriori* error estimates for the finite element method. *International Journal for Numerical Methods in Engineering*, **12**: 1597–1615, 1978.

[2] F.-J. Barthold, M. Schmidt, E. Stein. Error indicators and mesh refinement for finite-element-computations of elastoplastic deformations. *Computational Mechanics*, **22**: 225–238, 1998.

[3] CEB-FIP. *Model Code 1990, Bulletin d'Information.* CEB, Lausanne, Switzerland, 1990.

[4] C.A. Duarte, J.T. Oden. An *h-p* adaptive method using clouds. *Computer Methods in Applied Mechanics and Engineering*, **139**: 237–262, 1996.

[5] G. Hofstetter, H.A. Mang. *Computational Mechanics of Reinforced and Prestressed Concrete Structures.* Vieweg, Braunschweig, Wiesbaden, 1995.

[6] R. Lackner. *Adaptive finite element analysis of reinforced concrete plates and shells*, volume 89 of *Dissertationen an der Technischen Universität Wien.* Österreichischer Kunst- und Kulturverlag, Vienna, 2000. In print.

[7] R. Lackner, H.A. Mang. Adaptive FE ultimate load analysis of reinforced concrete plates and shells. In *CD-ROM Proceedings of the 1st Structural Engineers World Congress*, San Francisco, USA, 1998. Elsevier Science, Oxford.

[8] R. Lackner, H.A. Mang. Adaptive FEM for the analysis of concrete structures. In R. de Borst, N. Bićanić, H.A. Mang, G. Meschke, eds., *Computational Modelling of Concrete Structures, Proceedings of the EURO-C 1998 Conference*, volume 2, pages 897–919, Badgastein, Austria, 1998. Balkema, Rotterdam.

[9] R. Lackner, H.A. Mang. Adaptivity in computational mechanics of concrete plates and shells. *Mechanics of Cohesive-Frictional Materials*, 1999. Submitted for publication.

[10] R. Lackner, H.A. Mang. Error estimation in ultimate load analysis of reinforced concrete structures. In *CD-ROM Proceedings of the European Conference of Computational Mechanics*, Munich, Germany, 1999.

[11] L.-Y. Li, P. Bettess. Error estimates and adaptive remeshing techniques in elasto-plasticity. *Communications in Numerical Methods in Engineering*, **13**: 285–299, 1997.

[12] H.A. Mang. *Flächentragwerke*, Vol. 6 (*Rechenorientierte Baumechanik*) of *Der Ingenieurbau*, pp. 1–139. Ernst & Sohn, Berlin, 1995.

[13] H.A. Mang, Ch. Hellmich, R. Lackner, B. Pichler. Computational structural mechanics. In *CD-ROM Proceedings of the European Conference of Computational Mechanics*, Munich, Germany, 1999.

[14] MARC Analysis Research Corporation, Palo Alto, CA 94306. *MARC Reference Manual* – Vol. B: *Element Library*, August 1996. Multi-Purpose Finite Element Package.

[15] G. Meschke, Th. Huemer, H.A. Mang. Computer-aided retrofitting of a damaged RC cooling tower shell. *Journal of Structural Engineering (ASCE)*, **125**(3): 328–337, 1999.

[16] J. Peraire, M. Vahdati, K. Morgan, O.C. Zienkiewicz. Adaptive remeshing for compressible flow computations. *Journal of Computational Physics*, **72**: 449–466, 1987.

[17] D. Perić, J. Yu, D.R.J. Owen. On error estimates and adaptivity in elastoplastic solids: Applications to the numerical simulation of strain localization in classical and Cosserat continua. *International Journal for Numerical Methods in Engineering*, **37**: 1351–1379, 1994.

[18] N. Rehle, E. Ramm. Generieren von FE-Netzen für ebene und gekrümmte Flächentragwerke. *Der Bauingenieur*, **70**: 357–364, 1995.

[19] VGB, Technische Vereinigung der Großkraftwerksbetreiber, Essen, Germany. *Bautechnik bei Kühltürmen*, 1990.

[20] J.Z. Zhu, O.C. Zienkiewicz, E. Hinton, J. Wu. A new approach to the development of automatic quadrilateral mesh generation. *International Journal for Numerical Methods in Engineering*, **32**: 849–866, 1991.

[21] O.C. Zienkiewicz, J.Z. Zhu. A simple error estimator and adaptive procedure for practical engineering analysis. *International Journal for Numerical Methods in Engineering*, **24**: 337–357, 1987.

[22] O.C. Zienkiewicz, J.Z. Zhu. The superconvergent patch recovery and *a posteriori* error estimates. Part 1: The recovery technique. *International Journal for Numerical Methods in Engineering*, **33**: 1331–1364, 1992.